A Microwave Holography Methodology for Diagnostics and Performance Improvement for Large Reflector Antennas

D. J. Rochblatt
Ground Antennas and Facilities Engineering Section

Microwave holography has proven to be a powerful technique for various evaluations, diagnostics, and RF performance improvements for large reflector antennas. This technique utilizes the Fourier transform relation between the complex far-field radiation pattern of an antenna and the complex aperture field distribution. Resulting aperture phase and amplitude distribution data can be used to precisely characterize various crucial performance parameters, including panel alignment, panel shaping, subreflector position, antenna aperture illumination, directivity at various frequencies, and gravity deformation effects.

The methodology of the data processing presented in this article was developed at JPL and has been successfully applied to the DSN 34-m beam waveguide antennas. A companion article in this issue (Rochblatt and Seidel) describes the application of this technology to the DSS-13 antenna. The antenna performance was improved at all operating frequencies (wide-bandwidth improvement) by reducing the main reflector mechanical surface rms error to 0.43 mm. At Ka-band (32-GHz), the estimated improvement is 4.1 dB, resulting in an aperture efficiency of 52 percent. The performance improvement was verified by efficiency measurements and additional holographic measurements.

I. Introduction

Microwave holography is a measurement technique that has now been successfully applied to improve the performance of many types of reflector and array antennas throughout the world [1–7].[1] The raw data (the observable) for this technique is the complex far-field pattern of the antenna under test. For large reflector antennas, geostationary satellites are commonly used as convenient far-field signal sources. The beacon continuous wave (CW) signal from a geostationary satellite is usually used with a narrow-bandwidth receiver, while a transponder signal is usually the preferred choice for a wide-bandwidth receiver. Figure 1 presents a typical narrow-bandwidth receiver system architecture based on an HP 8510B analyzer and an external phase-locked loop (PLL) (with a variable PLL bandwidth of 1 to 20 Hz). The reference antenna is

[1] B. L. Seidel and D. J. Rochblatt, *DSS-13 Beam Waveguide Antenna Phase I Final Report*, JPL D-8451 (internal document), Jet Propulsion Laboratory, Pasadena, California, pp. 4.1–4.23, May 15, 1991.

needed as a phase reference for the measurement, as well as to keep the narrow-bandwidth receiver in phase lock with the carrier [8,9].

This article provides a detailed analysis of the unique methodology and data processing developed at JPL by the author.

II. Mathematical Algorithms

The mathematical relationship between an antenna far-field radiation pattern (T) and the antenna surface-induced current distribution (J) is given by the exact radiation integral [10]

$$\vec{T}(u,v) = \int\int_s \tilde{J}(x',y') \exp^{jkz'} [\exp^{-jkz'(1-\cos\theta)}] \times \exp^{j(ux'+vy')}\, dx'dy' \quad (1)$$

where

$z(x',y') =$ the surface s

$(u,v) =$ directional cosine space

$\theta =$ observation angle

For small observation angles ($\theta \cong 0$ deg) of the far-field pattern, this expression becomes a Fourier transform relationship

$$\vec{T}(u,v) = \int\int_s \tilde{J}(x',y') \exp^{jkz'} \exp^{jk(ux'+vy')}\, dx'dy' \quad (2)$$

To derive the residual surface error, geometrical optics-ray tracing is used to relate the small normal error, ϵ, directly to an aperture phase error in a main reflector paraboloid geometry (Fig. 2). In this small error approximation, it is assumed that the aperture phase error is entirely due to the projected surface errors. In addition, the three-dimensional structure of the surface error is not recovered; rather, an axial component equal to the average error over the resolution cell size is recovered. The normal error can then be computed using the paraboloid geometry. In practical application, when many resolution cells resolve a single panel, high accuracy (typically $\lambda/250$ at 12 GHz) can be achieved in determining panel setting screw adjustments. It can be computed from the geometry in Fig. 2

$$1/2\Delta PL \equiv 1/2[P'P + PQ]$$

$$= 1/2\left[\frac{\varepsilon}{\cos\phi} + \frac{\varepsilon\cos 2\phi}{\cos\phi}\right] = \varepsilon\cos\phi \quad (3)$$

$$\text{Phase}(\Delta PL) = \frac{4\pi}{\lambda}\varepsilon\cos\phi \quad (4)$$

and

$$\cos\phi = \frac{1}{\sqrt{1+\frac{Z}{F}}} \quad (5)$$

and for a paraboloid:

$$\cos\phi = \frac{1}{\sqrt{1+\frac{X^2+Y^2}{4F^2}}} \quad (6)$$

Allowing for the removal of a constant phase term and substituting Eq. (4) into Eq. (2) yields:

$$T(u,v) = \exp^{-j2kF} \int\int_s [|J(x',y')| \exp^{j4\pi^{\epsilon/\lambda}\cos\phi} \exp^{jkz'}] \times \exp^{jk(ux'+vy')}\, dx'dy' \quad (7)$$

where $[\ldots] \equiv J_e$ (equivalent current distribution).

For the processing of sampled data, the associated discrete Fourier transform (DFT) is utilized:

$$T(p\Delta u, q\Delta v) = sxsy \sum_{n=-N1/2}^{N1/2-1} \sum_{m=-N2/2}^{N2/2-1} J(nsx, msy) \times \exp^{j2\pi\left(\frac{np}{N1}+\frac{mq}{N2}\right)} \quad (8)$$

where

$N1, N2 =$ the measured data array size

$sx, sy =$ sampling intervals in the aperture coordinates

$n,\ m,\ p,\ q =$ integers indexing the discrete samples

$\Delta u, \Delta v =$ sampling intervals in u, v far-field space

Since the magnitude of the far-field pattern is essentially bounded, the fast Fourier transform (FFT) is usually used for computation, and is symbolized here by (F). Solving for the residual normal surface error and substituting Eq. (6) yields

$$\varepsilon(x,y) = \frac{\lambda}{4\pi}\sqrt{1+\frac{x^2+y^2}{4F^2}}\,\text{Phase}\left\{\exp^{j2kF}\,F^{-1}[T(u,v)]\right\} \tag{9}$$

The spatial resolution in the final holographic maps is defined at the 50-percent level of the Fourier transform of the truncation function [7,11]. Rectangular and triangular windowing are commonly used, with competing advantages to both. For rectangular windowing, the lateral resolution is derived [7,11]

$$\delta = \frac{D}{kN} \tag{10}$$

where

$D =$ main reflector diameter

$N =$ the square root of the total number of data points

$k =$ sampling factor, usually $0.5 < k < 1.0$

The lateral resolution is inversely proportional to the number of sidelobes measured. For the DSN 70-m antennas, the required resolution of 0.4 m is achieved with a data array size of 197 × 197. For the DSN 34-m antennas, the required resolution of 0.32 m is achieved with a data array size of 127 × 127 [12].

Figure 3 shows the complex Fourier transform relationship between the far-field and the aperture functions for a 34-m antenna (DSS 13). The far-field amplitude and phase, Figs. 3(a) and 3(b), respectively, are measured on rectangular coordinates of 127 × 127 with sampling intervals of 34.8 mdeg (the sampling factor is 0.84). Figures 3(c) and 3(d) show the aperture amplitude and surface error function with a lateral resolution of 0.32 m.

The accuracy in each resolution cell of the final holographic maps was formulated from a simulation study [9], which agrees well with analytically derived expressions [2]. In this study [9], Eq. (11) is derived

$$\sigma \cong 0.082\frac{\lambda D}{\delta SNR} \tag{11}$$

where

$\sigma =$ standard deviation (accuracy) in recovering the mean position of a resolution cell

$\lambda =$ wavelength

$SNR =$ beam peak voltage signal-to-noise ratio in the test (antenna) channel

The accuracy across the holographic map varies with the aperture amplitude illumination. The accuracy is better at the center of the dish and gradually becomes worse toward the edge, where the illumination falls off rapidly [9]. For a uniformly illuminated antenna design, the accuracy remains relatively constant, becoming quickly worse just at the edge, where the illumination falls off rapidly. Typically, accuracies of 0.05 mm to 0.10 mm were achieved with a corresponding SNR of 73 dB to 60 dB. Equation (11) also indicates that the accuracy is inversely proportional to the resolution. This is due to the larger averaging area available at the larger resolution cell, as expected.

The resulting aperture phase function (the dirty map) needs to be corrected for modulo-2π phase errors. These occur due to the small measurement wavelength and a large phase error that is partially due to pointing and subreflector position errors. Figures 4 and 5 are examples of aperture phase maps before and after correction of modulo-2π phase errors, respectively.

The next phase cleanup algorithm removes from the aperture function phase error components that are due to pointing and subreflector position errors. This can be done by fitting polynomials to the aperture phase data whose orders are equal to the expected order of the errors. Either the Zernike [13] or the modified Jacobi polynomials [14] can be used. Determination of pointing error-linear term, astigmatism, focus shift, coma, and spherical aberration are readily identified. The orthogonality properties of the Jacobi polynomial allow solving for its coefficients by

$$C_m^n = \frac{\zeta n}{2\pi}\int_0^1\int_0^{2\pi} \varepsilon(s',\phi')\cos(n\phi')F_m^n(s')s'ds'd\phi' \tag{12}$$

$$D_m^n = \frac{\zeta n}{2\pi}\int_0^1\int_0^{2\pi} \varepsilon(s',\phi')\sin(n\phi')F_m^n(s')s'ds'd\phi' \tag{13}$$

where

$\varepsilon(s',\phi') =$ surface error function

$\zeta_n =$ Neumann number

In addition, the above polynomials can be used to separate systematic (low-frequency) errors from random (high-frequency) error components by filtering (Fig. 6) [6].

Another technique for removing phase errors due to pointing and subreflector position errors has been developed via the global best fit paraboloid. Here, the entire data set is weighted-least-squares fitted to the paraboloid, permitting six degrees of freedom in the model, three vertex translations, two rotations, and a focal length change.

Minimization is performed on the sum squares of the residual path length changes S, given by

$$S = \sum_{i=1}^{N^2} \Gamma (\Delta PL_i)^2 A_i \tag{14}$$

where

Γ = support domain masking operator

ΔPL_i = path length change

A_i = amplitude weighting factor

The minimum for S is found by solving the six partial differential equations simultaneously

$$\left.\begin{aligned}
\frac{\partial S}{\partial x_0} &= 2\sum_{i=1}^{N^2} \Gamma \frac{\partial \Delta PL_i}{\partial x_0} \Delta PL_i A_i = 0 \\
\frac{\partial S}{\partial y_0} &= 2\sum_{i=1}^{N^2} \Gamma \frac{\partial \Delta PL_i}{\partial y_0} \Delta PL_i A_i = 0 \\
\frac{\partial S}{\partial z_0} &= 2\sum_{i=1}^{N^2} \Gamma \frac{\partial \Delta PL_i}{\partial z_0} \Delta PL_i A_i = 0 \\
\frac{\partial S}{\partial \alpha} &= 2\sum_{i=1}^{N^2} \Gamma \frac{\partial \Delta PL_i}{\partial \alpha} \Delta PL_i A_i = 0 \\
\frac{\partial S}{\partial \beta} &= 2\sum_{i=1}^{N^2} \Gamma \frac{\partial \Delta PL_i}{\partial \beta} \Delta PL_i A_i = 0 \\
\frac{\partial S}{\partial K} &= 2\sum_{i=1}^{N^2} \Gamma \frac{\partial \Delta PL_i}{\partial K} \Delta PL_i A_i = 0
\end{aligned}\right\} \tag{15}$$

where

$\left.\begin{matrix} X_0 \\ Y_0 \\ Z_0 \end{matrix}\right\}$ = vertex coordinates translation

α = rotation about the x-axis

β = rotation about the y-axis

and

$$K = \frac{1}{4}\left(\frac{1}{F} - \frac{1}{F'}\right) \tag{16}$$

where

F = focal length of the original paraboloid

F' = focal length of the best-fit paraboloid

The antenna surface axial rms error is then computed with respect to the position of the fitting paraboloid

$$RMS = \frac{\sqrt{\sum_{i=1}^{N} \Gamma (1/2 \Delta PL_i)^2}}{\sum_{i=1}^{N^2} \Gamma} \tag{17}$$

The subreflector position error is found via the six parameters computed above. Figure 7 presents a large linear phase error term due to pointing errors where errors due to subreflector position are minimal.

It is correct to apply the best-fit paraboloid algorithm to either the conventional Cassegrain paraboloid-hyperboloid or dual-shaped reflector systems, even though the latter do not use a paraboloid as the main reflector. Either design is a plane-wave-to-point source transformer, differing only in the field intensity distribution.

The resultant aperture function at the end of this process is defined here as the effective map since it includes all phase effects that are contributing to the antenna performance [15]. These frequency-dependent effects include the subreflector scattered (frequency-dependent) feed phase function and struts' diffraction effects. Removal of the feed phase function and subreflector support structure diffraction effects results in a frequency independent map, which is defined here as the mechanical map.

By deriving panel adjustment based on the effective map, the surface shape will conjugate to the phase errors, optimizing the performance of the antenna at a single frequency equal to the measurement frequency, while degrading the performance at all other frequencies. For antennas operating at a single frequency, this procedure is advantageous. However, many antennas (including the DSN's)

operate at several different frequencies and require wide-bandwidth performance. For these antennas, the mechanical map must be used to derive panel setting information.

Figure 8 is a feed phase function derived for the DSS-13 antenna, a 34-m beam-waveguide antenna at 12.198 GHz, using Geometrical Theory of Diffraction (GTD). Figure 9 is an effective map derived for the same antenna at 12.198 GHz. Subtracting the feed phase function from the effective map and masking the struts' diffraction effects resulted in the mechanical map presented in Fig. 10. Successful removal of the frequency-dependent feed phase function must result in reduction of the rms error for the mechanical map. This is due to the uniqueness of such a solution. As shown above, the rms decreased by 27.5 percent, from 0.98 mm to 0.71 mm.

Panel setting information is derived by sorting all the data points within each panel and performing a rigid-body least-squares fit. The algorithm allows for one translation and two rotations (S^k, α^k, and β^k), hence, a rigid body motion (Fig. 11). For each panel and its associated n data points, the motion parameters are solved via Eq. (18)

$$\begin{bmatrix} \sum_{i=1}^{n} \cos^2(\gamma_i) & \sum_{i=1}^{n} d_i \cos^2(\gamma_i) & -\sum_{i=1}^{n} e_i \cos(\gamma_i) \\ \sum_{i=1}^{n} d_i \cos^2(\gamma_i) & \sum_{i=1}^{n} d_i^2 \cos^2(\gamma_i) & -\sum_{i=1}^{n} e_i d_i \cos(\gamma_i) \\ -\sum_{i=1}^{n} e_i \cos(\gamma_i) & -\sum_{i=1}^{n} d_i e_i \cos(\gamma_i) & \sum_{i=1}^{n} e_i^2 \end{bmatrix} \times \begin{bmatrix} S^k \\ \alpha^k \\ \beta^k \end{bmatrix} = \begin{bmatrix} -\sum_{i=1}^{n} \varepsilon_i \cos^2(\gamma_i) \\ \sum_{i=1}^{n} \varepsilon_i d_i \cos^2(\gamma_i) \\ \sum_{i=1}^{n} \varepsilon_i e_i \cos^2(\gamma_i) \end{bmatrix} \quad (18)$$

This mathematical process increases the accuracy in determining the screw adjustment correction by a factor of $\sqrt{n}$, since all n data points within each panel are used to derive each screw adjustment. The three parameters from the least squares fit above are also used to recompute the predicted surface errors within each panel that will result after panel setting. Figures 12, 13, and 14 are, respectively, the before, predicted, and after mechanical maps derived during holographic measurements of DSS 13 and applying the above algorithms. The antenna was found to have an rms surface error of 0.88 mm, which was reduced to 0.45 mm. Figure 13, the predicted surface map (rms = 0.36 mm), indicates that panels in rings 8 and 9 were deformed, which was then confirmed in Fig. 14, the derived surface after panel setting.

The Appendix by S. Stewart, D. Rochblatt, and B. Seidel of the companion article in this issue describes in detail the cause for these deformed features due to using DSS-15 main reflector panels on the DSS-13 beam-waveguide (BWG) antenna. The reduction in rms from 0.88 mm to 0.45 mm was achieved within one session of panel setting, which limited the screw adjustments to the nearest 1/8 of a turn.[2] Figure 15 is a sample printout of the panel-setting screw-adjustment listing produced by this software package.

Another significant feature of the mechanical map is that surface tolerance efficiency can be computed at frequencies other than the measured one. This is possible since the aperture phase function has been cleaned of all effects that are frequency dependent. Surface tolerance efficiency can be computed by integrating the entire aperture function. In this computation, it is assumed that the aperture amplitude function is also frequency independent. The introduced error in this assumption is thus very small.

$$\eta(K)_{\text{surface}} = 20 \log_{10} \frac{\sqrt{\sum_{i=1}^{N^2} \Gamma 10^{ampdb_i/20} \cos\left[\phi_{m_i}\left(\frac{\lambda_m}{\lambda_k}\right)\right]^2 + \sum_{i=1}^{N^2} \Gamma 10^{ampdb_i/20} \sin\left[\phi_{m_i}\left(\frac{\lambda_m}{\lambda_k}\right)\right]^2}}{\sum_{i=1}^{N^2} \Gamma 10^{ampdb_i/20}} \quad (19)$$

where

ϕ_{m_i} = phase value at the measured frequency

sub k = any other frequency

An effective surface error ϵ can be computed by equating the above expression to that of Ruze [11,16]

[2] ibid.

$$\eta = \exp -(4\pi\varepsilon/\lambda)^2 \qquad (20)$$

Figure 16 shows the estimated surface loss versus frequencies of DSS 13 before and after panel setting, indicating a performance improvement of 4.1 dB at 32 GHz, which resulted in an aperture efficiency of 52 percent. Figure 17 shows the measured efficiency of the DSS-13 antenna before and after panel setting as a function of elevation angle at X-band (8.45 GHz). As shown in Fig. 17, the peak antenna gain increased by 0.21 dB and moved from the antisymmetric 57-deg elevation to the desired 45-deg elevation that was specified as the required antenna rigging angle.

Figure 18 is a gravity deformation of DSS 13 between the elevation angles of 12.7 deg and 46.5 deg. Gravity deformation maps are highly important in deriving accurate structural deformation models for large reflector antennas. It is observed from this image (Fig. 18), that the bypass shroud on the right side of the antenna is exerting a force in the outer axial direction, creating the observed signature. It was found that the disturbing shroud forces are attributed to eccentricity of the shroud axes of rotation with respect to the antenna elevation axis.[3] The eccentricity is also confirmed by dial-indicator measurements. Figure 19 presents the major software components of the microwave holography methodology in a block diagram.

[3] R. Levy, *DSS-13 Antenna Structure Measurements and Evaluation*, JPL D-8947 (internal document), Jet Propulsion Laboratory, Pasadena, California, October 1, 1991.

Acknowledgments

The author would like to thank Dan Bathker for his numerous helpful technical discussions and contributions. In addition, the author wishes to thank Boris Seidel and Manuel Franco from JPL and Paul Wright and Eric Schoessow from Eikontech, Ltd., for helping with the holographic measurements at DSS 13.

References

[1] A. P. Anderson, J. C. Bennett, A. J. T. Whitaker, and M. P. Godwin, "Measurement and optimization of a large reflector antenna by microwave holography," *Proc. Int. Conf. on Ant. and Prop.*, IEE Publication no. 169, pp. 128–131, London, England, 1978.

[2] P. F. Scott and M. Ryle, "A rapid method for measuring the figure of a radio telescope reflector," *Mon. Not. Roy. Astr. Soc.*, vol. 178, pp. 539–545, 1977.

[3] J. C. Bennet, A. P. Anderson, P. A. McInnes, and A. J. T. Whitaker, "Microwave holographic metrology of large reflector antennas," *IEEE Trans. Antennas and Propagat.*, vol. AP-24, no. 3, pp. 295–303, May 1976.

[4] M. P. Godwin, A. J. T. Whitaker, and A. P. Anderson, "Microwave diagnostics of the Chilbolton 25m antenna using OTS satellite," *Proc. Inst. Elec. Eng. Int. Conf.*, York, England, pp. 232–236, 1981.

[5] C. E. Mayer, J. H. Davis, W. L. Peters, and W. J. Vogel, "A holographic surface measurement of the Texas 4.9-meter antenna at 86 GHz," *IEEE Trans. Instru. Meas.*, vol. IM-32, no. 1, pp. 102–109, March 1983.

[6] D. J. Rochblatt, "Holographic measurements of 34 and 70m DSN antennas," *Antenna optics metrology workshop W.2*, presented at the URSI/IEEE-AP-S symposium, London, Ontario, Canada, June 28, 1991.

[7] D. J. Rochblatt and B. L. Seidel, "DSN Microwave Antenna Holography," *TDA Progress Report 42-76*, vol. October–December 1983, Jet Propulsion Laboratory, Pasadena, California, pp. 27–42, February 15, 1984.

[8] D. J. Rochblatt, "System Analysis for DSN Microwave Antenna Holography," *TDA Progress Report 42-97*, vol. January–March 1989, Jet Propulsion Laboratory, Pasadena, California, pp. 132–157, May 15, 1989.

[9] D. J. Rochblatt and Y. Rahmat–Samii, "Effects of Measurement Errors on Microwave Antenna Holography," *IEEE Transactions on Antennas and Propagation*, vol. 39, no. 7, pp. 933–942, July 1991.

[10] Y. Rahmat-Samii, "Surface diagnosis of large reflector antennas using microwave metrology—An iterative approach," *Radio Science*, vol. 19, no. 5, pp. 1205–1217, September–October 1984.

[11] C. E. Mayer, J. H. Davis, and H. D. Foltz, "Texas 5-m antenna aperture efficiency doubled from 230–300 GHz with error compensating secondary," *IEEE Trans. Antennas and Propagat.*, vol. AP-39, no. 3, pp. 309–317, March 1991.

[12] D. J. Rochblatt, "System requirements for NASA Deep Space Network microwave antenna holography," paper presented at International Symposium on Antenna and Propagation, Tokyo, Japan, August 22–25, 1989.

[13] M. Born and E. Wolf, *Principles of Optics*, Oxford: Pergamon Press, pp. 464–468, 1965.

[14] V. Galindo-Israel and R. Mittra,"A new series representation integral with application to reflector antennas," *IEEE Trans. Antennas Propagat.*, vol. AP-25, pp. 631–635, September 1977 (correction in *IEEE Trans. Antennas Propagat.*, vol. AP-26, p. 628, July 1978).

[15] D. J. Rochblatt, Y. Rahmat-Samii, and J. H. Mumford, "DSN Microwave Antenna Holography Part II: Data Processing and Display of High Resolution Effective Maps," *TDA Progress Report 42-87*, vol. July–September 1986, Jet Propulsion Laboratory, Pasadena, California, pp. 92–97, November 15, 1986.

[16] J. Ruze, "Antenna tolerance theory—A review," *IEEE Proc.*, vol. 54, pp. 663–640, April 1966.

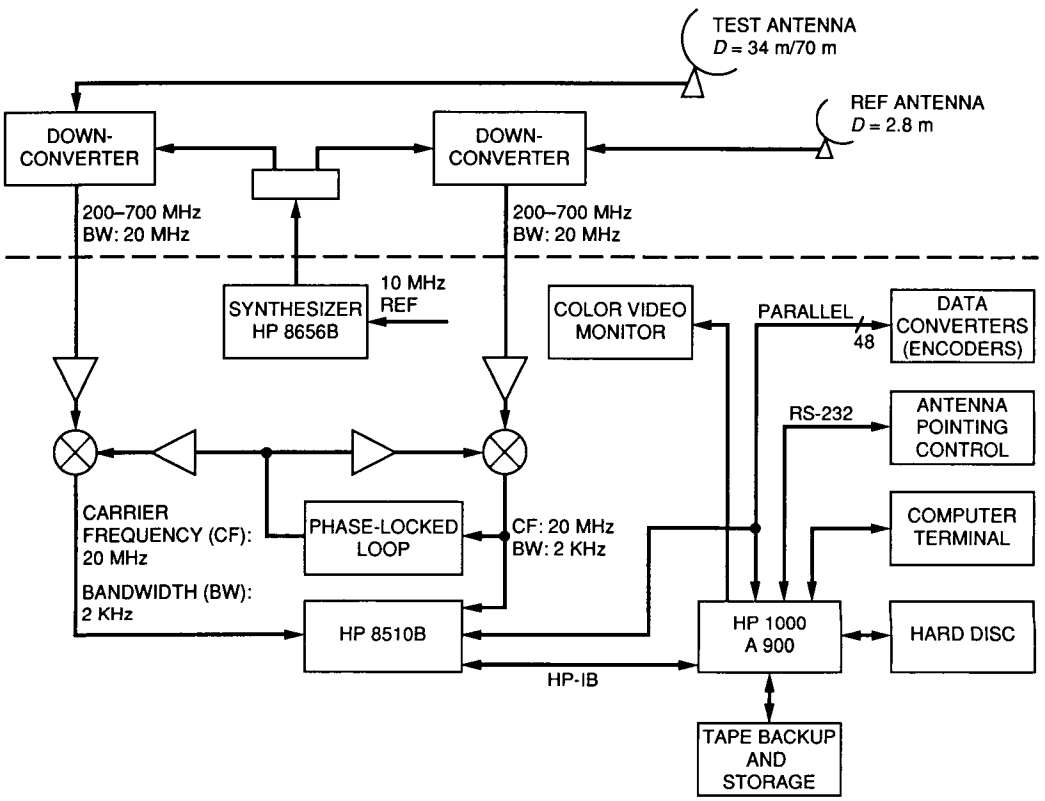

Fig. 1. The holographic measurement using a reference antenna.

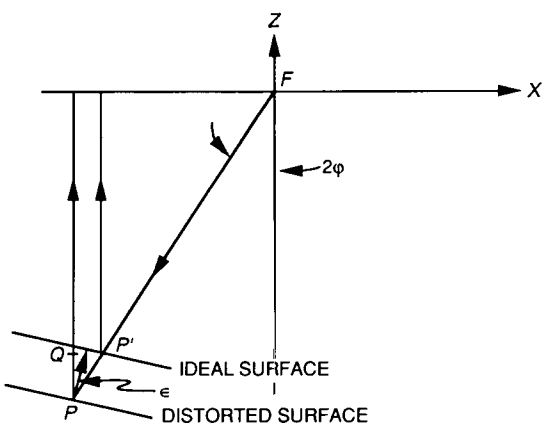

Fig. 2. Surface distortion geometry.

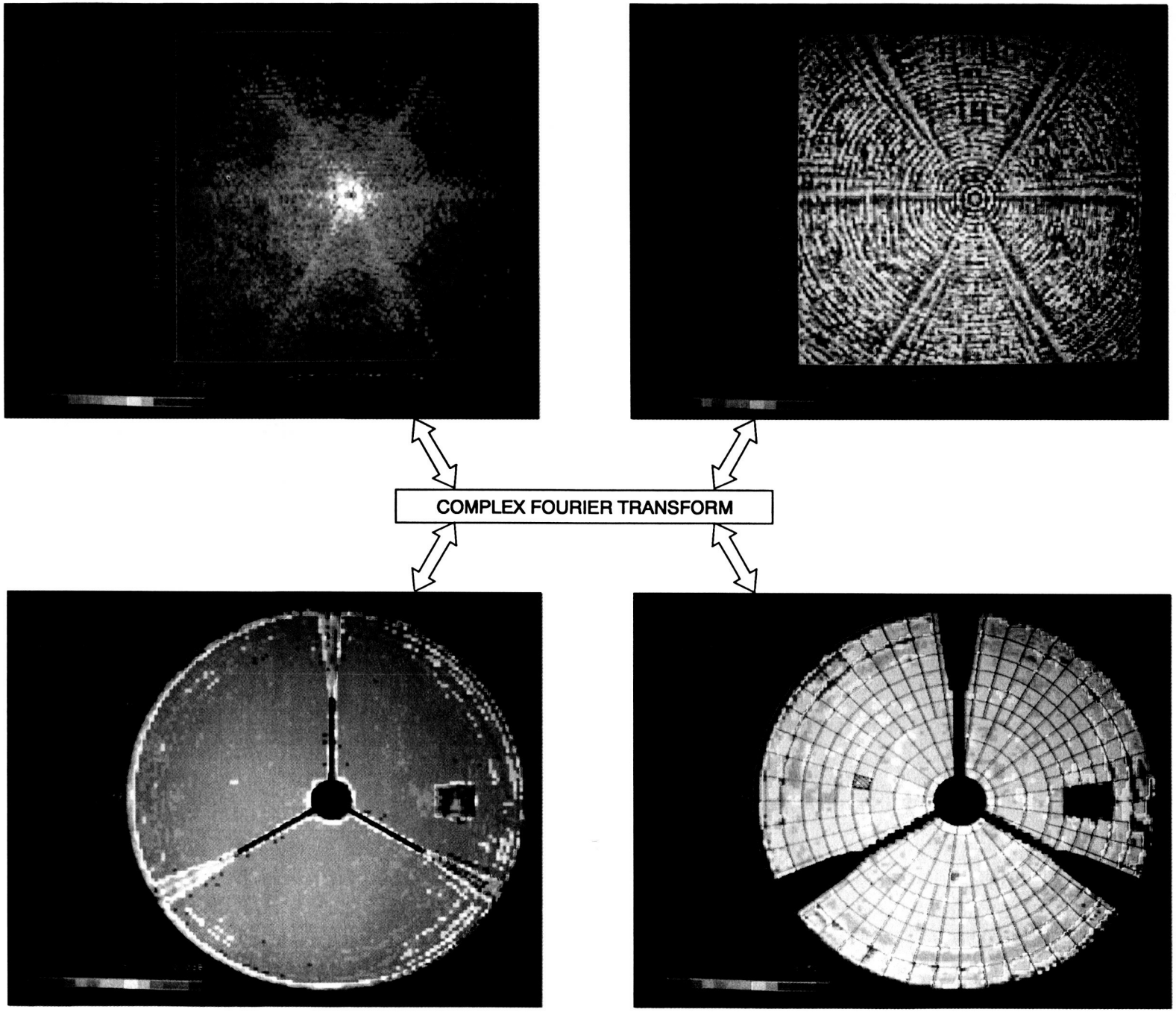

Fig. 3. Complex Fourier transform relating the antenna far-field and aperture functions.

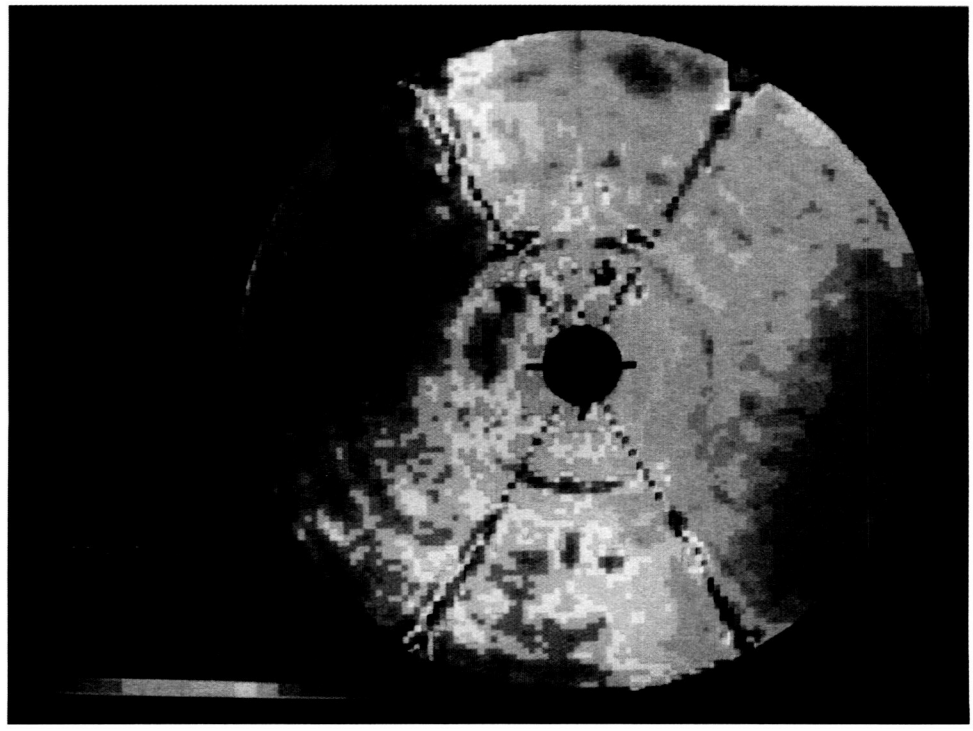

Fig. 4. Phase map before correction for modulo 2π.

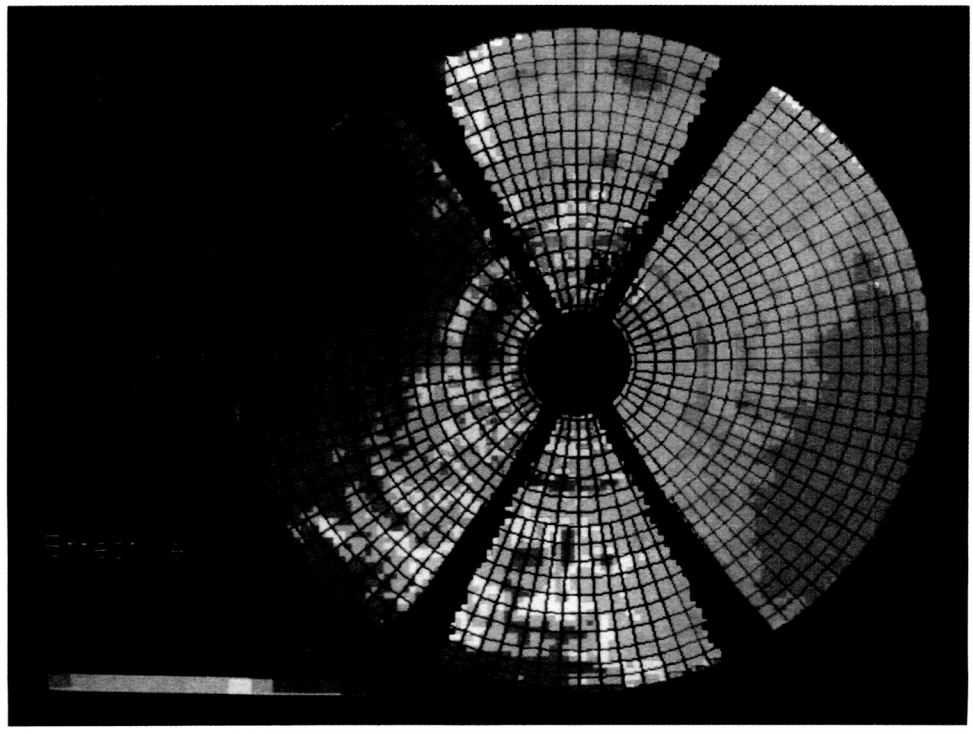

Fig. 5. Phase map after correction for modulo 2π.

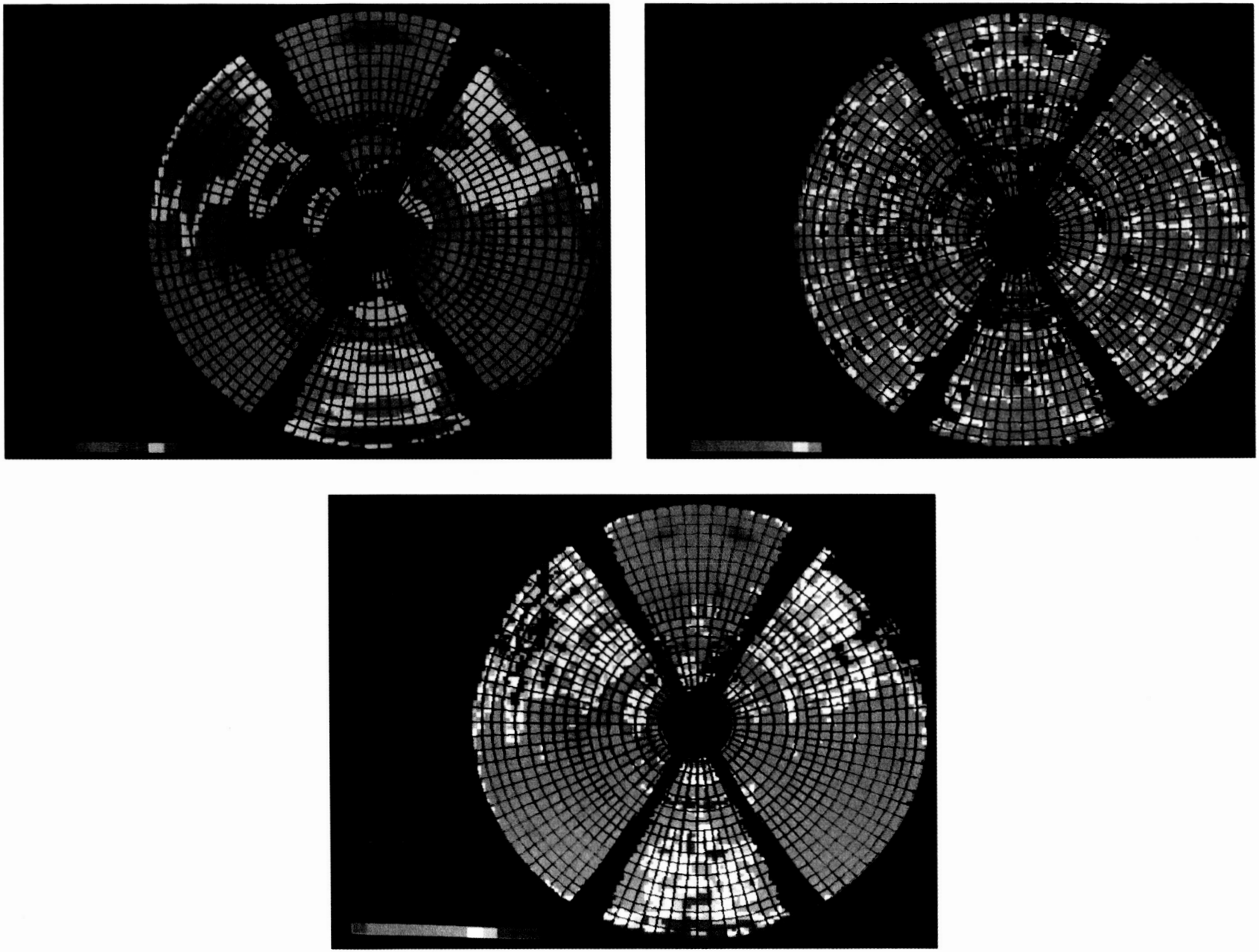

Fig. 6. Modified Jacobi polynomial decomposition separates structural deformation from panel setting errors.

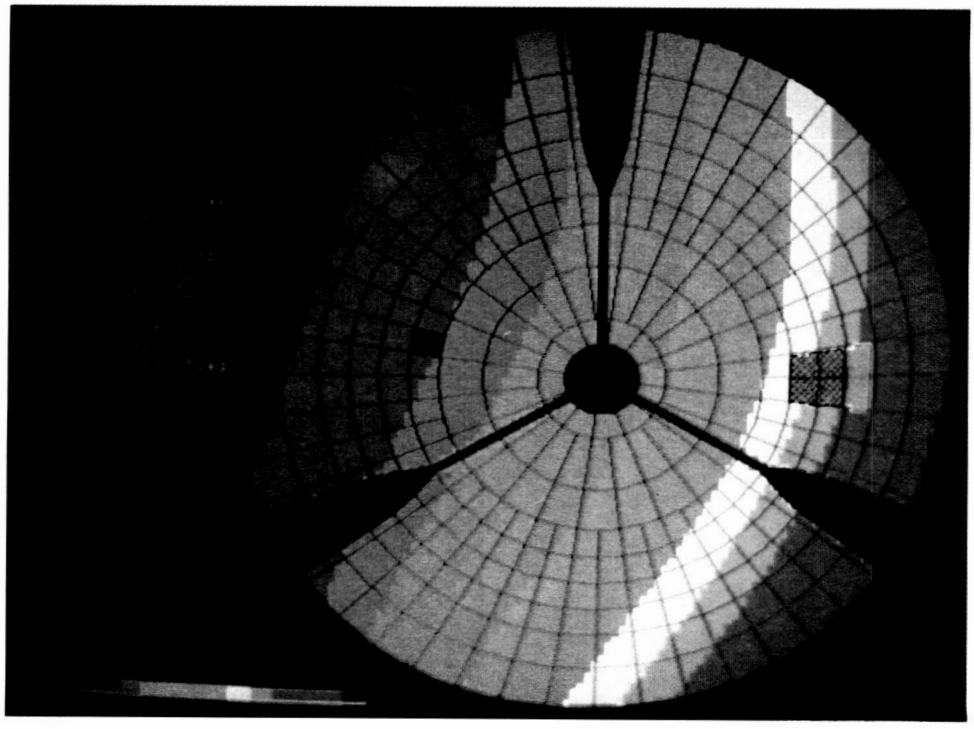

Fig. 7. Phase map due to pointing and subreflector position errors.

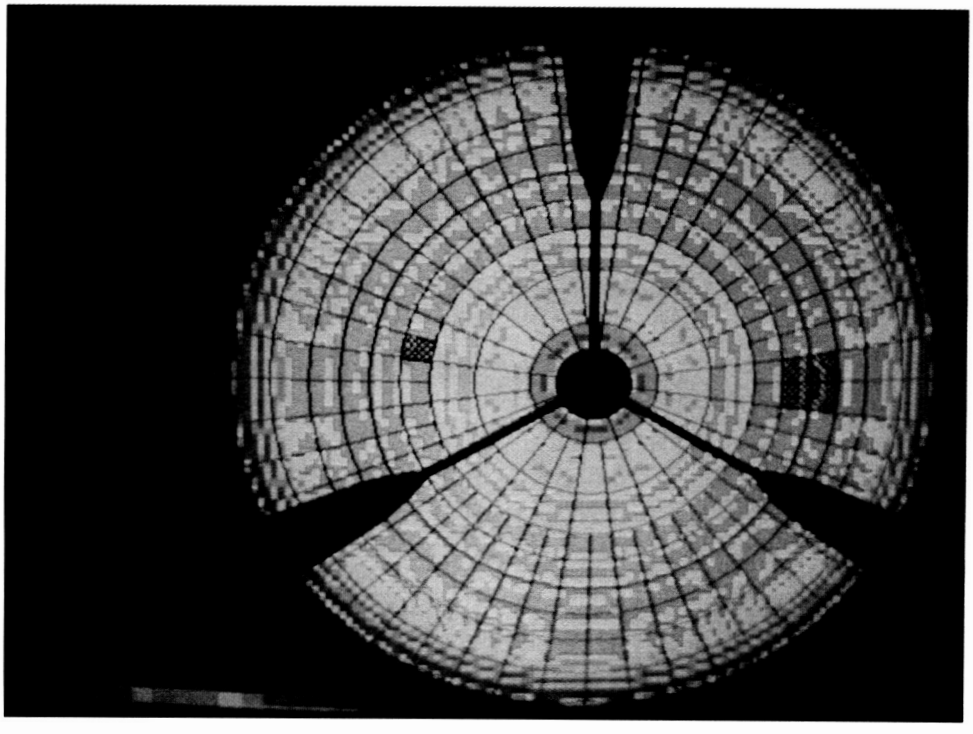

Fig. 8. Feed phase function for DSS-13 34-m antenna at 12.198 GHz.

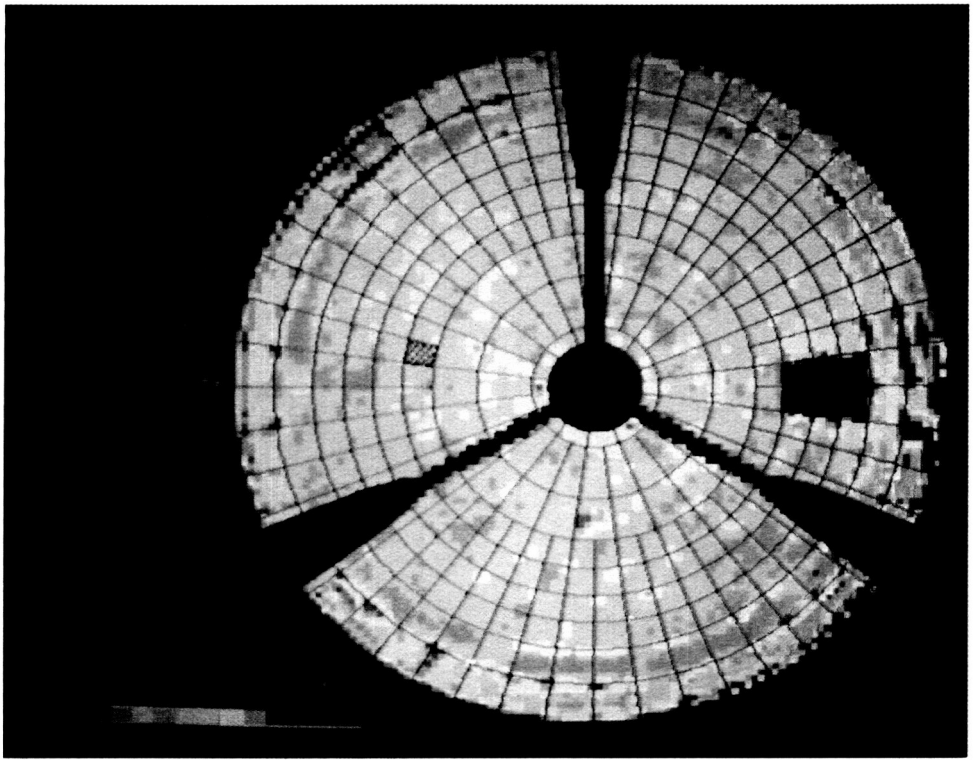

Fig. 9. Effective map.

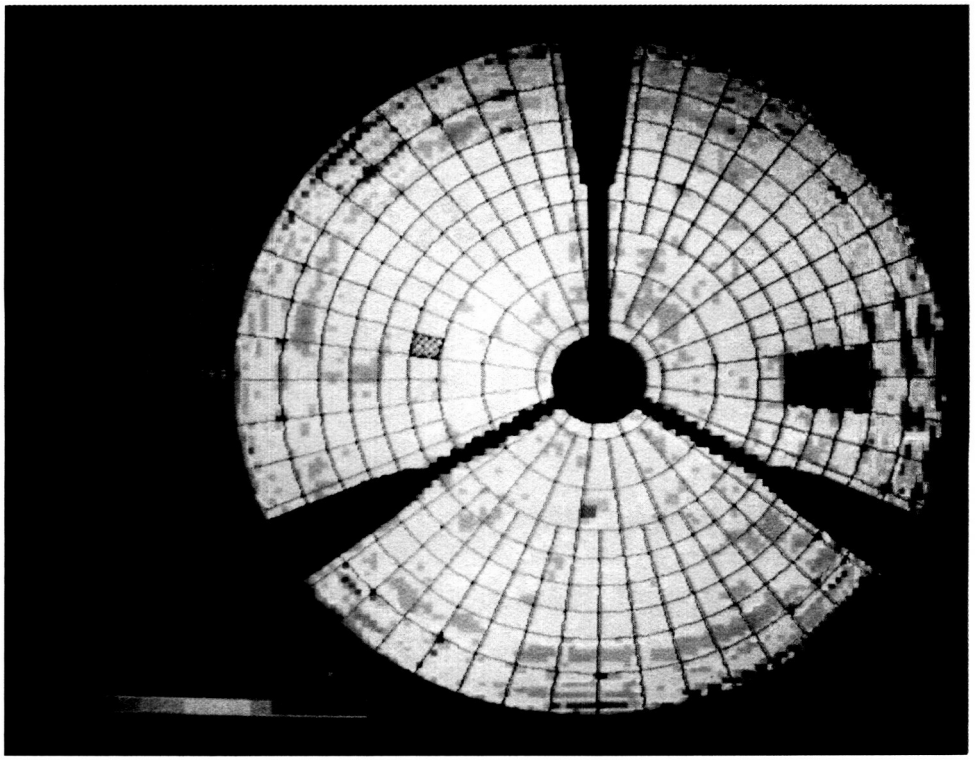

Fig. 10. Mechanical map.

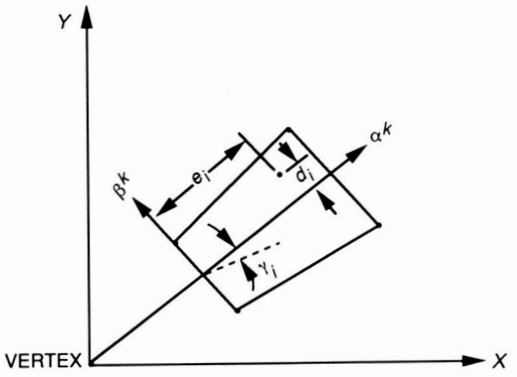

Fig. 11. Rigid-body panel motion modeling.

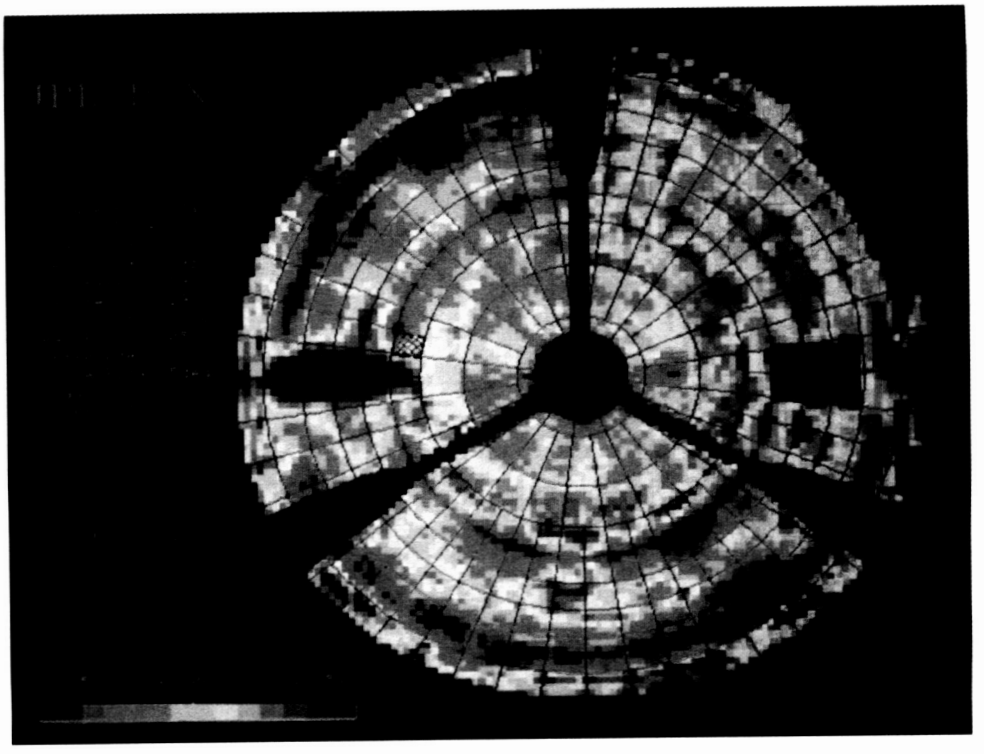

Fig. 12. DSS-13 mechanical surface as found.

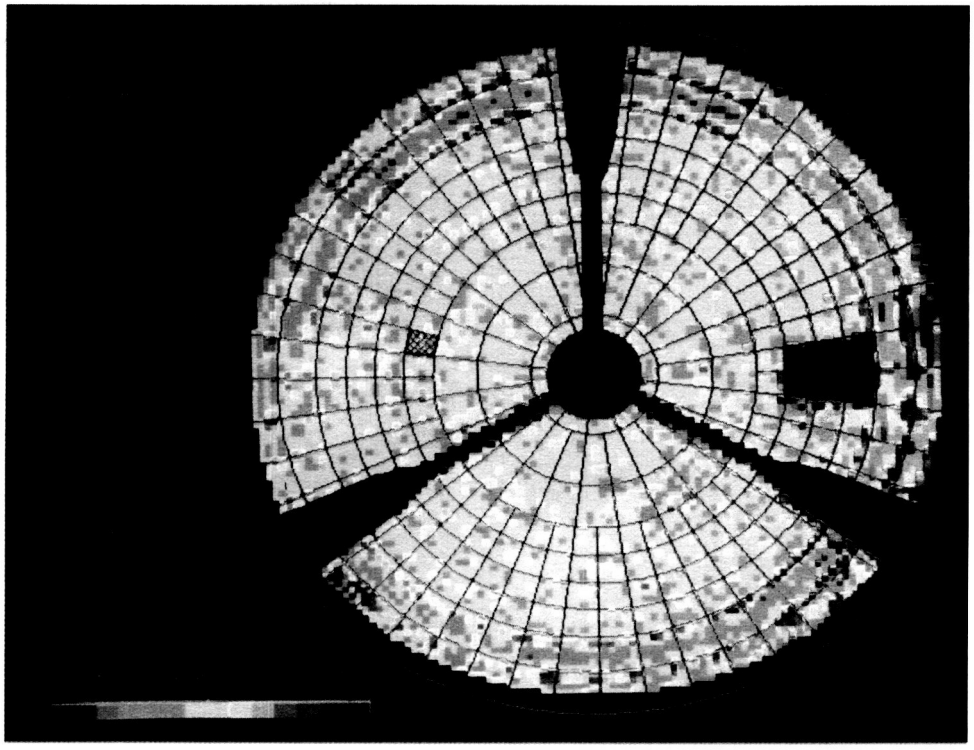

Fig. 13. DSS-13 computer-predicted mechanical surface based on methodology.

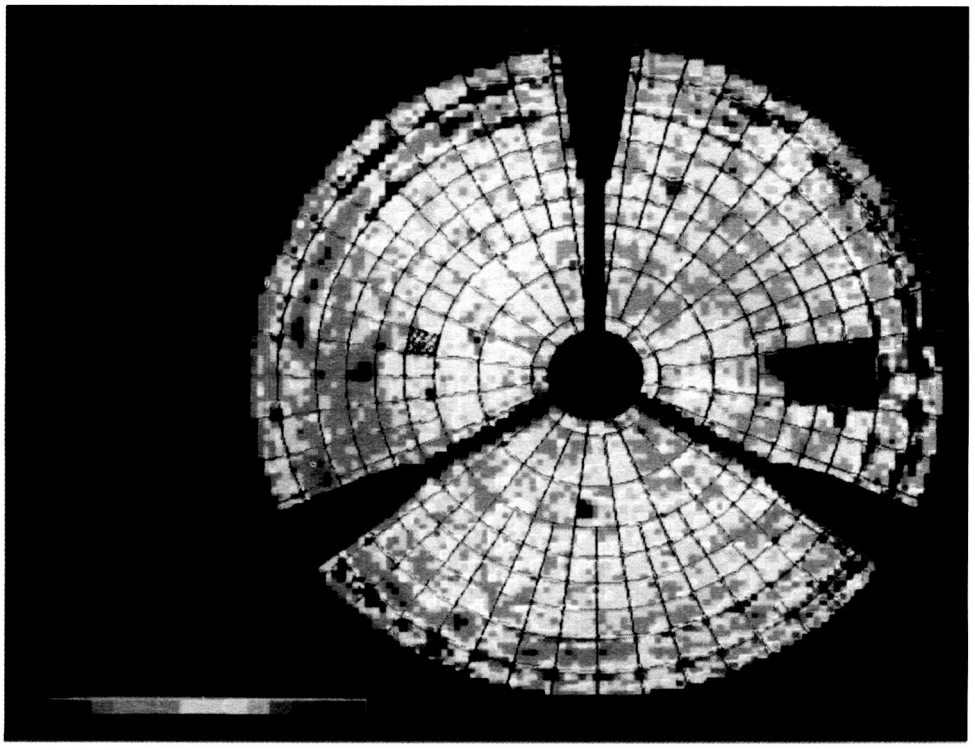

Fig. 14. DSS-13 mechanical surface after panel setting.

SCREW ADJUSTMENTS FOR RING 1

PANEL	A	B	C	D	E	F
1	0.0464	0.0309	0.0171	0.0065	0.0325	
2	0.0296	0.0047	−0.0006	−0.0047	0.0243	
3	0.0172	0.0071	0.0146	0.0204	0.0248	
4	0.0473	0.0096	0.0084	0.0075	0.0461	
5	0.0296	−0.0044	0.0179	0.0350	0.0521	
6	0.0507	0.0213	0.0110	0.0031	0.0403	
7	0.0593	0.0232	0.0303	0.0358	0.0665	
8	0.0808	0.0837	0.0441	0.0135	0.0407	
9	0.0374	0.0089	0.0229	0.0337	0.0515	
10	0.0654	0.0300	0.0258	0.0226	0.0611	
11	0.0306	0.0230	0.0261	0.0284	0.0337	
12	0.1012	0.1022	0.0494	0.0087	0.0478	

SCREW ADJUSTMENTS FOR RING 2

PANEL	A	B	C	D	E	F
1	0.0412	0.0224	0.0077	0.0142	0.0275	0.0446
2	0.0150	0.0242	0.0313	0.0020	0.0009	−0.0004
3	−0.0050	0.0027	0.0086	0.0038	−0.0012	−0.0075
4	0.0009	0.0012	0.0015	0.0099	0.0079	0.0054
5	0.0114	0.0116	0.0117	0.0138	0.0132	0.0125
6	0.0188	0.0071	−0.0020	0.0087	0.0156	0.0244

Fig. 15. Panel-setting screw-adjustments (inches) computer listing for DSS-13 34-m antenna derived from scan JPL106 127 × 127.

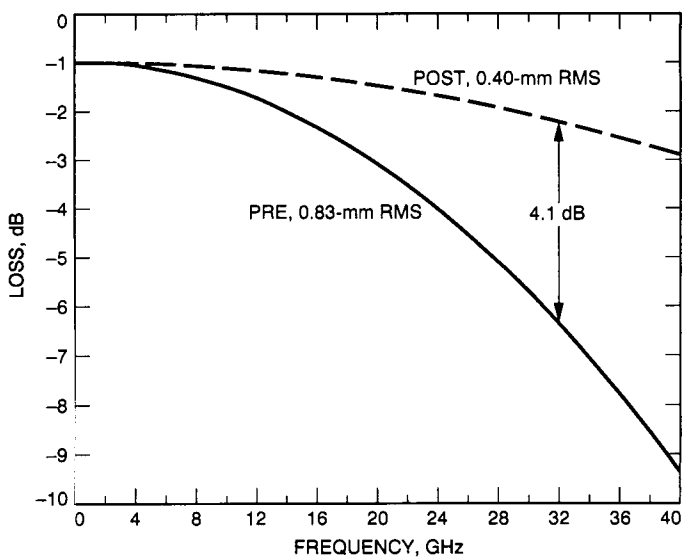

Fig. 16. Estimated DSS-13 surface loss.

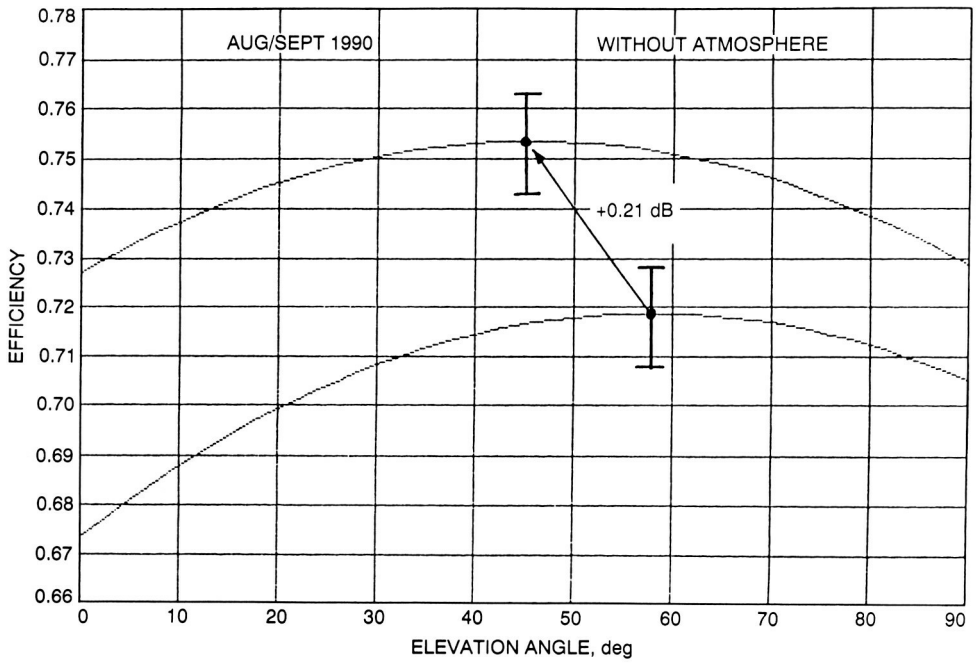

Fig. 17. DSS-13 X-band (8.45-GHz) efficiency at the Cassegrain focus before (bottom) and after (top) application of the holography methodology.

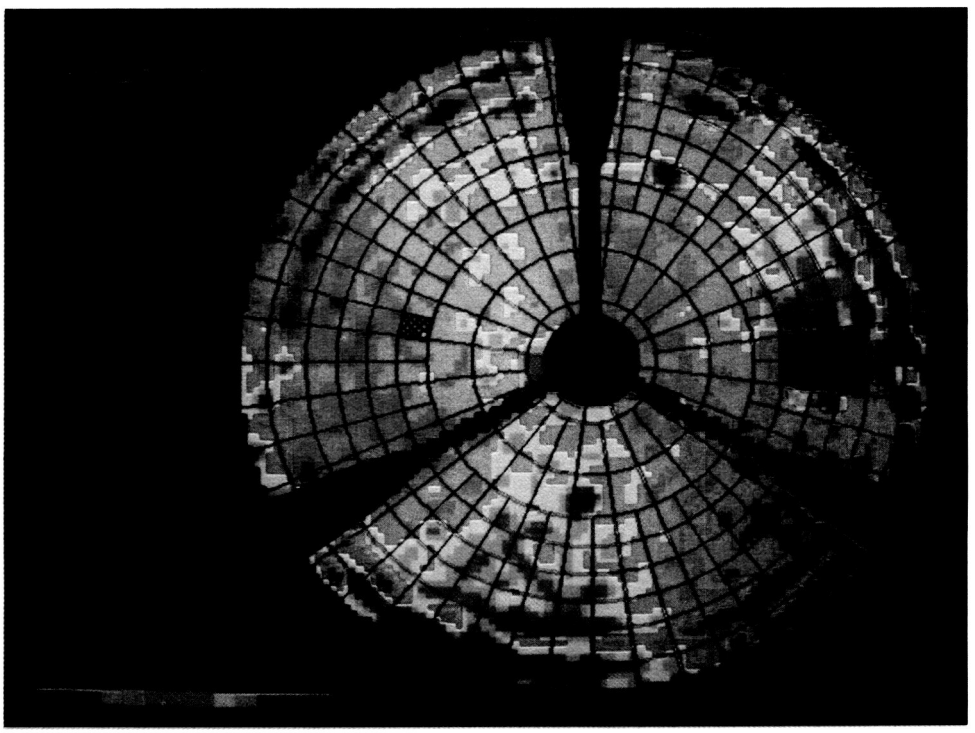

Fig. 18. Gravity deformation signature derived for DSS 13 from measurements at two elevation angles (12.7–46.5 deg).

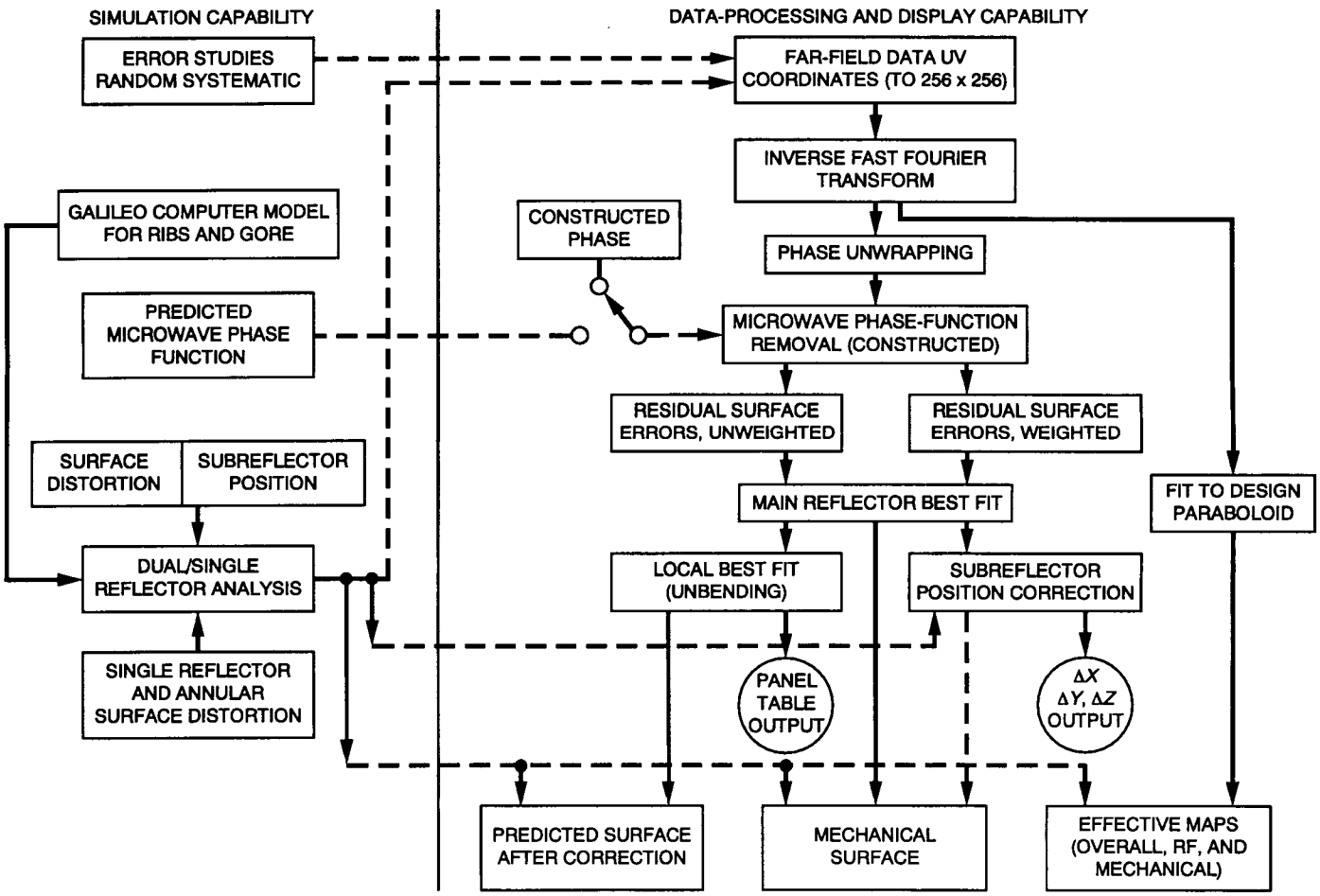

Fig. 19. Simplified block diagram of the microwave holography software methodology.